

A DEEPER LOOK INTO X-RAY-SELECTED
AGN CANDIDATES IN DWARF GALAXIES
WITH CHANDRA

by

Adonis Arismendy Sanchez

A thesis submitted in partial fulfillment
of the requirements for the degree

of

Master of Science

in

Physics

MONTANA STATE UNIVERSITY
Bozeman, Montana

June 2023

©COPYRIGHT

by

Adonis Arismendy Sanchez

2023

All Rights Reserved

DEDICATION

I dedicate this work to my mother and father for doing their best to forge a life for me where I could learn and explore to my heart's content even in this hostile land.

ACKNOWLEDGEMENTS

I would like to thank my advisor, Dr. Amy Reines, for giving me the opportunity to engage in the field of astrophysics and for supporting me on my journey in graduate school. I would also like to thank my wonderful family and amazing friends. You all have been instrumental in my quest for higher learning and allowing me to pursue even the smallest of my curiosities. Thank you.

TABLE OF CONTENTS

1. INTRODUCTION	1
Importance of Understanding Supermassive Black Holes (SMBH)	1
Formation Mechanisms	2
The Problem and Solutions to Direct Observations.....	3
AGNs in Dwarf Galaxies and X-rays.....	6
X-ray Telescopes and Surveys.....	7
eROSITA on the SRG	7
The eROSITA Final Equatorial Depth Survey	7
The eROSITA All-Sky Survey.....	8
Chandra X-ray Observatory	8
2. A CHANDRA VIEW OF EROSITA-SELECTED AGN CANDIDATES IN DWARF GALAXIES	11
Contribution of Authors and Co-Authors	11
Manuscript Information	12
Introduction	13
Sample of Dwarf Galaxies	14
Observations and Data Reduction.....	18
Analysis and Results.....	20
X-ray Sources.....	20
X-ray Spectra.....	24
Possible Origins of the X-ray Emission.....	27
X-ray Binaries.	27
Ultraluminous X-ray Sources.	27
Massive Black Holes.	29
Comparison with Latimer et al. (2021a).....	29
Summary and Conclusions	31
3. CONCLUSION	33
REFERENCES CITED.....	36

LIST OF TABLES

Table	Page
2.1 Sample Galaxy Properties.....	17
2.2 Chandra Observations	19
2.3 X-Ray Sources	22
2.4 X-ray Source Properties From Fitting.....	26

LIST OF FIGURES

Figure	Page
1.1 A simplified model of an AGN's structure. The thin accretion disk surrounding the black hole is responsible for the X-ray and ultraviolet radiation observed. Surrounding the accretion disk, an obscuring torus made of hot dust produces infrared radiation. Above and below the central engine, there are clouds of ionized gas comprising the broad and narrow line regions. The broad line region is responsible for the broadening of emission lines in optical spectra. Lastly, the accretion disc may produce jets of charged particles emitting in the radio, X-ray, and even gamma due to synchrotron radiation and inverse Compton scattering.....	5
2.1 Left: Three-color images of our target galaxies retrieved from the Dark Energy Camera Legacy Survey (DECaLS; Dey et al. 2019) with the z , r , and g bands depicting red, green, and blue respectively. Right: <i>Chandra</i> X-ray images of the galaxies in the 2-10 keV band. We show the positions and the corrected combined positional uncertainty (based on the <code>RADEC_ERR_CORR</code> parameter from the eFEDS main catalog) in magenta. We also overlay the positions of our detected X-ray sources as red crosses. The green circles represent the $\sim 2''$ apertures around the sources. The red circle shows our new positional uncertainties regarding the X-ray sources. As can be seen, each one falls within the positional uncertainty reported in the eFEDS main catalog, except ID 1 which shows one of the off-galaxy X-ray sources detected.....	16
2.2 Hardness ratio vs. \log 2–10 keV X-ray luminosity for our two galaxies with a detected X-ray source in at least one of the two bands. The hardness ratio was calculated using BEHR (see Section 2). The error bars are the 68% confidence intervals. Hardness ratios for unabsorbed $\Gamma = 1.8, 2.0$, and 2.5 are depicted as solid gray lines, while the absorbed power laws with $\Gamma = 1.8$ are shown with gray dashed lines.	23

LIST OF FIGURES – CONTINUED

Figure	Page
2.3 Summary of X-ray spectral fitting with reported Γ and intrinsic absorption values for the X-ray sources in ID 2 and ID 3. Left: X-ray source spectrum of ID 2. We fit the spectrum with an absorbed power-law model, finding a best fit $\Gamma = 2.75$ and $N_{H,int} = 0.247 \times 10^{22} \text{ cm}^{-2}$. Right: X-ray source spectrum of ID 3. We find the spectrum with an absorbed power-law model, finding the best fit $\Gamma = 1.74$ and $N_{H,int} = 0.069 \times 10^{22} \text{ cm}^{-2}$	25
2.4 Total observed X-ray luminosities of the galaxies in our sample vs. what we would expect to see from XRBs via the relation of Lehmer et al. (2010). The black points are the values found by Latimer et al. (2021a) for comparison. The dashed line represents the one-to-one relation, and the scatter of 0.34 dex in the expected XRB luminosities is shown in grey to the bottom right. The error bars shown are 90% confidence intervals calculated via <code>srcflux</code> . Note: ID 1 is plotted using the upper limit of its minimum log luminosity.	28

ABSTRACT

The ability to accurately discern active massive black holes (BHs) in local dwarf galaxies is paramount to understanding the origins and processes of “seed” BHs in the early universe. We present *Chandra X-ray Observatory* observations of a sample of three dwarf galaxies ($M_* \leq 3 \times 10^9 M_\odot$, $z \leq 0.15$) pre-selected by Latimer et al. (2021a) as candidates for hosting active galactic nuclei (AGN). The galaxies were selected from the NASA-Sloan Atlas (NSA) with spatially coincident X-ray detections in the eROSITA Final Equatorial Depth Survey (eFEDS). Our new *Chandra* data reveal X-ray point sources in two of the three galaxies with luminosities of $\log(L_{2-10\text{keV}}/[\text{erg s}^{-1}]) = 39.1$ and 40.4. In the target galaxy with the non-detection, we calculate an upper limit on the luminosity for a potential source. We observed notably higher fluxes and luminosities from the two detected X-ray sources compared to their original eFEDS observations, pointing to possible X-ray variability on the scale of a few years. We plot and fit the spectra of the X-ray sources with a power-law model, finding the likely presence of intrinsic absorption. The X-ray luminosities are above that expected from XRBs, but we cannot definitively rule out stellar-mass compact objects with the data on hand. Assuming the X-ray sources are accreting massive BHs with masses that scale with the stellar mass of the host galaxies, the Eddington ratios are on the order of a few $\times 10^{-3}$.

INTRODUCTION

For decades we have know of the ubiquitous nature of supermassive black holes (SMBH) of masses $10^6 M_{\odot} < M_{BH} < 10^9 M_{\odot}$ housed in the cores of massive galaxies (Kauffmann et al., 2003; Reines, 2022; Volonteri, 2010). From observations of young quasars in early galaxies, we know of SMBHs having formed over relatively short cosmological times (hundreds of millions of years) such as Fan et al. (2006), Mortlock et al. (2011), and Bañados et al. (2018), however it is unknown how these SMBHs came to be. In contrast, the formation mechanisms for nearby or more modern stellar-mass black holes is well-understood as the end product of a specific path within the stellar evolution of massive stars. It has led many in the community to pursue work in trying to understand the formation mechanism(s) and development of such early SMBH (Inayoshi et al., 2020). As such, some theories have been developed to explain the creation and evolution of black hole seeds that would eventually grow to become SMBHs. A number of techniques have also arisen to find and study celestial objects that serve as present-day analogs of black hole seeds in the early universe.

Importance of Understanding Supermassive Black Holes (SMBH)

SMBHs are found in the cores of nearly all massive galaxies in the Universe. They are as fundamental a component to galactic structure as stars and the interstellar medium. SMBHs are the engines that drive active galactic nuclei (AGN) which present a source of feedback in their host galaxies, quenching its growth (Kelly & Merloni, 2012). It has also been shown that the mass of a SMBH appears to correlate strongly with various galaxy properties illustrating an intricate link between SMBHs and galactic evolution, yet the origins of these SMBH are shrouded in mystery. Understanding the origins of SMBHs would give us more insight into a

range of astrophysical phenomena such as tidal disruptions events (TDEs) and gravitational waves, as well as the growth of galaxies themselves, as mentioned prior. At some point in the the early cosmos, relatively smaller black holes (BHs) between $10^2 M_\odot$ and $10^6 M_\odot$ had to have existed and grown into the 10^9 -solar mass regime. These intermediate-mass black holes may tell us a great deal about how massive these initial "seeds" that grew into SMBHs were, how they formed, and in what kinds of environments they resided. It would give us a window into answering the key questions of how galaxies and their central BHs grow together and how they exactly influence each other.

Formation Mechanisms

We, at present, do not understand how the first seed BHs formed, but there has been much work over the years to address this problem theoretically and the environments that they must have grown from (see Latif & Ferrara 2016 for a review). Various mechanisms describing the formations of seed BHs have come about in the time since before we were even fully convinced on the existence of black holes. Each formation scenario is not without its caveats, but a few have gained prominence despite the case. The most popular scenarios are core-collapse from the first generation of massive stars, the collapse of hot, metal-free gas clouds, and the gravitational runaway of dense nuclear star clusters.

Population III (Pop III) stars in the early universe ($z \sim 20 - 30$) would have been metal-free and massive from the inability of molecular hydrogen to cool (Bromm & Larson, 2004; Karlsson et al., 2013) and could possibly leave behind SMBH seeds of $\sim 100 M_\odot$ (e.g., Fryer et al., 2001) but would either need to be much larger, experience a sustained growth at the Eddington limit, or undergo a few episodes of super-Eddington accretion during their lifespans (Jiang et al., 2019) if they are to grow to presently observed SMBH sizes.

The direct collapse of massive proto-galactic gas clouds bypassing stellar evolution would yield seed BHs of $\sim 10^4 - 10^6 M_\odot$ (e.g., Lodato & Natarajan, 2006). The direct

collapse scenario would require that it occurs at very high redshifts ($z < 10$) such that the gas is pristine or metal-free to prevent it from cooling or fragmenting (see Inayoshi et al. 2020 for a review). To be viable, the direct collapse pathway necessitates that the gas remains hot by either one of a list of proposed factors, such as assuming an elevated Lyman-Werner (ionizing) background (e.g., Latif et al., 2013; Omukai, 2001), photons from nearby star formation (Visbal et al., 2014), or heating through merger events (Wise et al., 2019).

The third channel through which SMBH seeds could arise producing BHs of masses $\sim 10^2$ – $10^4 M_\odot$ is from a gravitational runaway event within dense star clusters. In general, the center of the cluster collapses creating a high-density environment triggering a series of runaway stellar collisions that results in the creation of a massive BH. Depending on the timescales at which the process occurs, either ~ 100 Myr to 1 Gyr or a few million years denoted as the slow and fast scenarios respectively, determine the exact nature of the gravitational runaway. In the slow scenario, a stellar mass BH forms in the center of the cluster and then grows through mergers of with other BHs that have come about through typical stellar evolution. The fast scenario is described by massive stars falling to the center of the cluster and merging until the now much more massive star collapses into a BH of $\sim 1000 M_\odot$ (Inayoshi et al., 2020).

The Problem and Solutions to Direct Observations

In an ideal scenario, we would simply observe high-redshift galaxies in the early universe, collect the necessary data and catalogue the mass ranges of these SMBH seeds, but alas these galaxies are too dim and far off for direct observation, at least based on our current technology. As luck would have it, there is a class of celestial objects known as dwarf galaxies with low masses and relatively quiet merger histories that may contain black holes with masses analogous to SMBH seeds. Their stellar masses are usually defined as being similar to the Large Magellanic Cloud (Reines et al., 2013) with $M_* \lesssim 10^{9.5} M_\odot$. Dwarf galaxies allow

us to remedy the issues with observing early-universe galaxies with our current technology given that they are both numerous and found relatively close-by making observations far less challenging. Dwarf galaxies may play host to ancient BH seeds from the early universe. Based on observations, we would be able to gain information about a range of both galaxy and BH properties, or even determine the dominant formation mechanism(s) for SMBH seeds. In the past, the existence of massive BHs being hosted in dwarf galaxies was a subject of much controversy and debate. Yet within the last decade, we have obtained significant and meaningful evidence of BHs residing in not just a few dwarf galaxies, but large survey samples of them (Reines et al., 2013, 2011).

When detecting SMBHs there are a few typical methods employed. We can track the orbits of individual stars around the Galactic Center, but this is only feasible in the Milky Way since incredibly high spatial resolution would be required to view the individual orbits of stars in other galaxies. Reaching past our own galaxy, dynamical modeling of stellar or gas kinematics is possible for galaxies that are nearby but with the condition that we can resolve the region near the BH (i.e., the sphere of influence). The most efficient by far, especially for the purpose of detecting BHs in dwarf galaxies, is detecting the radiative signatures that coincide with accreting BHs. In other words, detecting and studying the light from AGNs is necessary in the low-mass regime.

AGNs commonly exhibit a set of traits including substantial emission that is non-thermal nor a consequence of stellar activity, particularly in the radio and X-ray continuum. The light we see is typically concentrated in a galaxy's center and may be highly variable with timescales ranging from just a few minutes to years. A virtue of AGNs is that they radiate light across the whole of the electromagnetic spectrum, all a consequence of the accretion onto a BH at its core. A model of an AGN is shown in Figure 1.1.

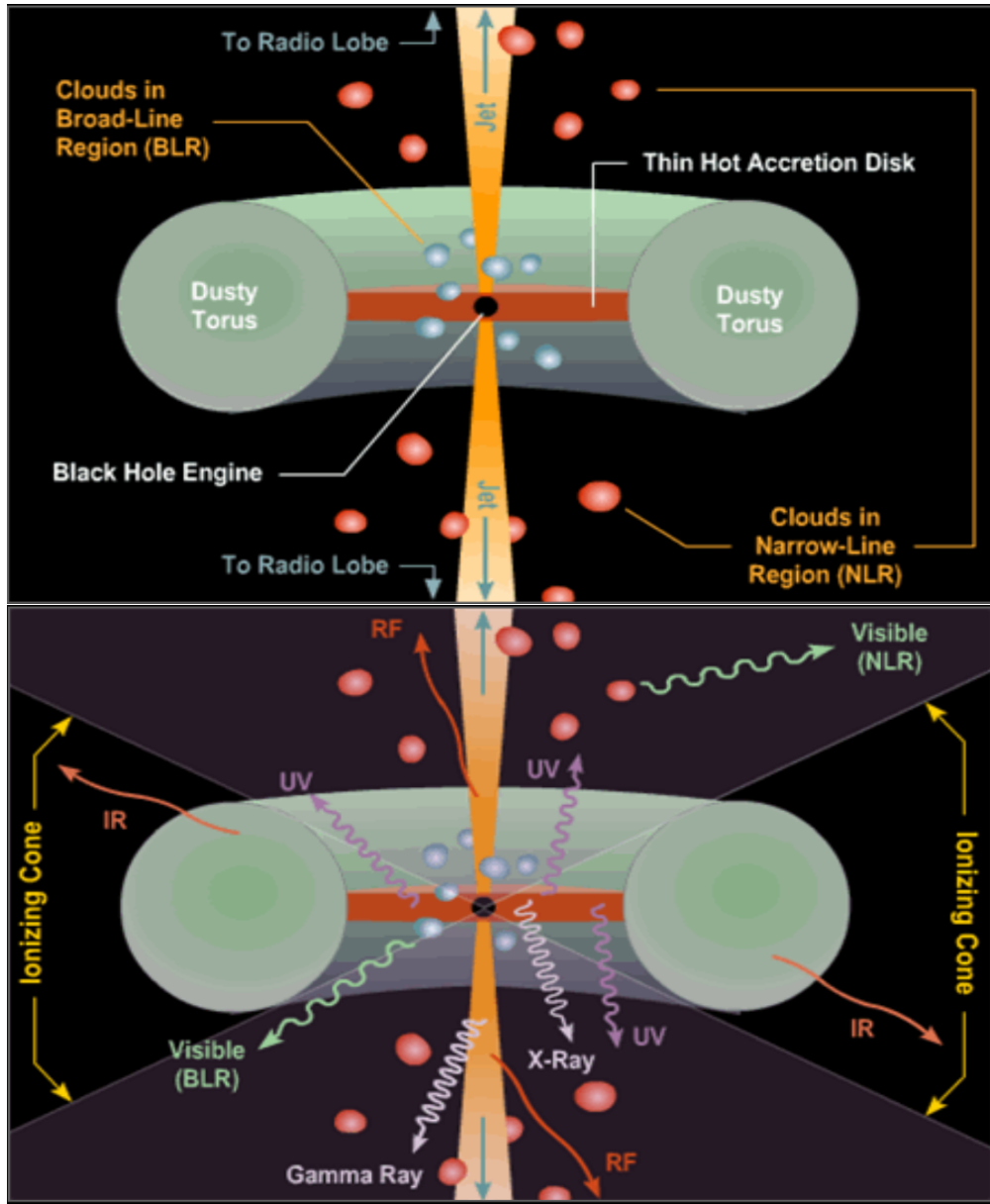


Figure 1.1: A simplified model of an AGN's structure. The thin accretion disk surrounding the black hole is responsible for the X-ray and ultraviolet radiation observed. Surrounding the accretion disk, an obscuring torus made of hot dust produces infrared radiation. Above and below the central engine, there are clouds of ionized gas comprising the broad and narrow line regions. The broad line region is responsible for the broadening of emission lines in optical spectra. Lastly, the accretion disk may produce jets of charged particles emitting in the radio, X-ray, and even gamma due to synchrotron radiation and inverse Compton scattering.

AGNs in Dwarf Galaxies and X-rays

Observing AGNs at various wavelengths permits us to identify active BHs in dwarf galaxies using a variety of techniques. X-ray observations in particular serve as a powerful tool since accretion onto black holes invariably produces X-rays, which are mostly unburdened by obscuring dust (Brandt & Alexander, 2015). X-rays can be utilized in detecting black holes with low accretion rates (Gallo et al., 2008) and are less susceptible to contamination from their host even in star-forming galaxies (Kimbrow et al., 2021; Reines et al., 2016). Lowly accreting black holes will also produce more hard X-rays by proportion (Ho, 2008). Specifically, hard X-rays are able to bypass obscuration from the dusty torus (Mushotzky, 2004). While X-rays offer a promising way to detect active BHs, AGNs in dwarf galaxies tend to exhibit luminosities that are orders of magnitude lower than AGNs in their more massive relatives making searches challenging (at all wavelengths).

Almost a decade ago this sub-field was spurred on by the discovery of a massive black hole in the dwarf starburst galaxy Henize 2-10 using a multiwavelength approach (Reines et al., 2011). X-ray data from the *Chandra X-ray Observatory* proved essential in revealing an X-ray point source coinciding with a central radio source (Reines et al., 2016). Subsequent X-ray studies have detected/confirmed a growing sample of massive black holes in dwarf galaxies (e.g. Baldassare et al. 2017; Latimer et al. 2021a,b; Lemons et al. 2015; Nucita et al. 2017; Pardo et al. 2016) and continue to do so today.

The thesis will focus on using *Chandra* X-ray observations to help verify AGN candidates in dwarf galaxies previously found by Latimer et al. (2021a) using X-ray data from the eROSITA Final Equatorial Depth Survey (eFEDS). The subsections below will provide a summary of the eROSITA X-ray Telescope, its mission, and the *Chandra X-ray Observatory*. In Chapter 2, we use X-ray observations from the *Chandra X-ray Observatory* to verify the AGN candidates in three dwarf galaxies found within the eFEDS catalogue by Latimer et al. (2021a). With the high-resolution X-ray data from *Chandra* we are able to

better discern the properties of the X-ray sources present in the galaxy and apply meaningful constraints on whether an AGN is truly present within these galaxies. This work is to be published in the *Astrophysical Journal*. Finally, in Chapter 3, we summarize our work and form conclusions based on our findings. We discuss the difficulties present in the search of AGN in dwarf galaxies utilizing X-rays and present future paths for research.

X-ray Telescopes and Surveys

eROSITA on the SRG

The extended ROentgen Survey with an Imagine Telescope Array (eROSITA; Predehl et al. 2021) is a wide-field X-ray telescope and the main instrument onboard the Spectrum-Roentgen-Gamma (SRG) space observatory developed and built by the Max Planck Institute for Extraterrestrial Physics (MPE) in Germany. It was successfully launched on July 13, 2019 and set on an orbit about the second Lagrange point (L2), roughly 1.5 million kilometers from Earth. From there, the X-ray telescope is performing the first imaging all-sky survey over the course of four years.

Unlike current X-ray telescopes such as Chandra and XMM-Newton, which have relatively small fields of view for the purpose of deep, pinpoint observations, the eROSITA has a large field of view for the purpose of wide-area surveys or all-sky in its case.

While the angular resolution is much coarser than *Chandra*, it is ideal for scanning massive portions of the Universe within a relatively small amount of time. Wide-field X-ray telescopes and their advantages have been discussed and utilized (e.g. Truemper 1993) for decades and eROSITA is the newest among them. eROSITA is sensitive from ~ 0.2 - 0.8 keV, with average on-axis resolution of $\sim 16''$ at 1.5 keV. (Predehl et al., 2021).

The eROSITA Final Equatorial Depth Survey The eROSITA Final Equatorial Depth Survey (eFEDS) was conducted during the telescope performance verification in early

November of 2019 prior to the all-sky survey. eFEDS covered $\sim 140 \text{ deg}^2$ of the sky, divided into four $\sim 35 \text{ deg}^2$ rectangular sub-fields (see Figure 1 in Brunner et al. 2022 for a visualization). The footprint coincides with a number of optical, near-infrared, imaging and spectroscopic surveys (e.g. HSC Wide Area Survey, Mezcua et al. 2018; DESI Legacy Imaging Survey, Dey et al. 2019; GAMA, Hickox et al. 2009; SDSS, She et al. 2017). The eFEDS catalog contains 27,910 X-ray sources in the 0.2-2.3 keV energy range, with a point source flux limit of $6.5 \times 10^{-15} \text{ erg cm}^{-2} \text{ s}^{-1}$ in the 0.5-2 keV band. The eFEDS catalog has a source density 70 times larger than the ROSAT ALL-Sky survey (Reines et al., 2016) and 2.5 times smaller than the XMM-XLL survey (Mezcua et al., 2018).

The eROSITA All-Sky Survey The eROSITA All-Sky Survey (eRASS; Predehl et al. 2021) is the primary mission of eROSITA on the SRG. The telescope began its four-year long scan of the entire sky in December 13, 2019, roughly a month after the eFEDS was conducted, and by the end of this year it will have accomplished 8 complete six month long scans of the celestial sphere. In its totality, the eRASS will be approximately 25 times more sensitive than the ROSAT ALL-Sky Survey in the soft (0.2-2.3 keV) X-ray band. In the hard (2.3-8 keV) X-ray band it will provide the first true imaging survey of the sky in this range. It is expected to yield a sample of ~ 3 million AGNs with a median redshift of $z \sim 1$ (Kolodzig et al. 2013) and ~ 1350 of those within dwarf galaxies (Latimer et al. 2021a). The survey will be able to provide monumental insights into X-ray binaries, active stars, and the evolution of supermassive black holes.

Chandra X-ray Observatory

First proposed in 1976 with funding beginning the following year, the *Chandra X-ray Observatory* launched in July 23, 1999 along with Space Shuttle Columbia. It is one of NASA's Great Observatories. Its outstanding ability to capture sub-arcsecond X-ray images and high resolution spectra have made it an indispensable asset to astronomy and X-ray

astronomy in their entirety. Chandra has the best angular resolution of any X-ray telescope to date. It is a necessity for multiwavelength studies in the search for AGNs in dwarf galaxies.

Chandra is able to view the complex structures within our universe with incredible detail, optimally designed to view the X-rays from high-energy regions. Given its expanded energy range of 0.2-10 keV, it has combined energy bands that in the past would have required different instruments. Chandra provides four-dimensional data for each X-ray photon detected, recording its energy, time, and the sky position which allows for imaging, timing, and spectroscopic analysis.

The Chandra X-ray Observatory consists of three parts: the X-ray telescope that focuses X-rays from celestial bodies, the scientific instrumentation that creates the data products from the X-rays collected for analysis, and the spacecraft itself providing the foundation required for the former two to function. The telescope itself or the High Resolution Mirror Assembly (HRMA) is comprised of four pairs of nested hyperboloid and paraboloid Wolter Type-I mirrors. They achieve an angular resolution of roughly 0.5 arcseconds, which equates to an angular resolution approximately 12 times better than XMM-Newton and 50 times that on ROSAT. It uses the small reflection angles and iridium coating on the mirror to achieve this high energy response. The mirrors have an effective area of 400 square centimeters at 1 keV with a focal length of 10 meters and a 1 degree field-of-view.

The scientific instruments aboard Chandra are the High Resolution Camera (HRC) and the Advanced CCD Imaging Spectrometer (ACIS). ACIS has 10 CCD chips across two arrays. The four of those chips in a 2×2 array is ACIS-I and other six in a 1×6 array is ACIS-S. ACIS-I is optimized for imaging wide (16×16 armin) fields, while ACIS-S is utilized for both imaging or a readout for the High Energy Transmission Grating (HETG). The ACIS-S together with the HETG reach a resolving power ($E/\Delta E$) up to 1000 from 0.4 - 10 keV. HETG is well-suited for detailed line diagnostics due to its high spectral resolution. HRC is a microchannel plate hosting two detectors: GRC-I for imaging and HRC-S for

spectroscopy. With a field-of-view of 31×31 arcmin, HRC-I has the the largest field-of-view of the instruments available on Chandra and is able to extend to energies lower than ACIS. Each one of these can be utilized to obtain deeper and high resolution data to conduct initial or follow-up observations of targets detected using other wavelengths or lower resolution X-ray telescopes.

Chandra started a revolution in the realm of X-ray astronomy imaging breath-taking astronomical phenomena and celestial bodies, collecting spectra and observing light curves over the past two decades. Again it guides us, peering deeper into previously X-ray-selected AGN candidates found within the eFEDS catalog to determine the nature of the X-ray sources that lie within.

A CHANDRA VIEW OF EROSITA-SELECTED AGN CANDIDATES IN DWARF GALAXIES

Contribution of Authors and Co-Authors

Manuscript in Chapter 2

Author: Adonis A. Sanchez

Contributions: Reduced and analyzed X-ray data, wrote initial draft of manuscript.

Author: Amy E. Reines

Contributions: Advised, helped edit manuscript, provided both editorial and scientific comments on the manuscript.

Author: Akos Bogdan

Contributions: Assisted in analyzing X-ray data, provided scientific and editorial comments on the manuscript.

Author: Ralph Kraft

Contributions: Utilized guaranteed time on *Chandra* to obtain the data. Provided scientific and editorial comments on the manuscript.

Manuscript Information

Adonis A. Sanchez, Amy E. Reines, Akos Bogdan, Ralph Kraft

The Astrophysical Journal Letters

Status of Manuscript:

☒ Prepared for submission to a peer-reviewed journal

☐ Officially submitted to a peer-reviewed journal

☐ Accepted by a peer-reviewed journal

☐ Published in a peer-reviewed journal

IOP Publishing

Introduction

It is well-understood and documented that massive black holes (BHs) with masses $10^6 \lesssim M_{\text{BH}}/M_{\odot} \lesssim 10^9$ inhabit the centers of nearly all massive galaxies. A portion of these BHs exhibit accretion, emit light across the electromagnetic spectrum, and are luminescent as active galactic nuclei (AGNs). As we reach toward lower mass scales ($M_{\star} \lesssim 10^9 M_{\odot}$; $M_{\text{BH}} \lesssim 10^5 M_{\odot}$) the fraction of dwarf galaxies hosting massive BHs/AGNs becomes much less certain. However, these systems are paramount as they may provide meaningful constraints on the seeding model(s) for the formation of the first generation of BHs in the early Universe (e.g., Greene et al., 2020; Reines, 2022; Volonteri, 2010). They also are representative of an early stage in the growth of massive BHs and provide an avenue for studying the effects of BH feedback at low masses (Silk, 2017).

Presently, there has been consistent growth in the evidence supporting massive BHs in dwarf galaxies found via various selection techniques, such as optical emission line spectroscopy, optical variability, mid-IR colors, and radio observations (for a review, see Reines, 2022). Each of these methods are not without their drawbacks. Optical search methods tend to be biased toward more massive BHs with higher Eddington fractions and galaxies with low star formation rates. Mid-IR colors suffer from contamination of dwarf starburst galaxies mimicking AGN signatures. Finally, the sensitivities of current radio surveys may miss a significant fraction of the population.

X-ray observations are able to bypass many issues presented by other techniques given that they are particularly effective at detecting active BHs with low Eddington ratios (Gallo et al., 2008; Hickox et al., 2009; Ho, 2008) or those in galaxies with active star formation (Kimbro et al., 2021; Reines et al., 2016; She et al., 2017). X-ray studies have been conducted in the past to not only search for AGNs in dwarf galaxies, but to also explore the BH occupation fraction and to place AGN-candidates in dwarf galaxies under further scrutiny

to confirm their presence. For example, Lemons et al. (2015) found candidate AGNs in local dwarf galaxies ($z < 0.055$; $M_* \lesssim 10^{9.5} M_\odot$) from archival data within the Chandra Source Catalog, and a similar study was conducted by Birchall et al. (2020) with the 3XMM catalog. Follow-up observations by Thygesen et al. (2023) aimed to verify the nature of the AGNs for three dwarfs within the sample found by Lemons et al. (2015) using high resolution *Chandra* and *HST* observations.

In this study, we re-examine and probe three nearby dwarf galaxies using high spatial resolution *Chandra* X-ray observations, which were previously found to host one nuclear or off-nuclear X-ray source per galaxy. These three targets come from a sample of six originally identified by (Latimer et al., 2021a) based on a determination of the AGN fraction from X-ray observations within the eROSITA Final Equatorial Depth Survey (eFEDS; Brunner et al. 2022). This work will help provide a meaningful example of what will be capable upon the release of the eROSITA All-Sky Survey (eRASS) in regards to the search and understanding of AGNs in dwarf galaxies.

Sample of Dwarf Galaxies

Our target galaxies were selected from the study of Latimer et al. (2021a) where from a parent sample of 63,582 local dwarf galaxies ($z \leq 0.15$, $M_* \leq 3 \times 10^9 M$) from the NASA-Sloan Atlas (v1_0_1) they find 495 of these galaxies fall within the 140 deg² (Brunner et al., 2022) eFEDS sky coverage. From here, they cross-match the $\sim 28,000$ X-ray sources in the eFEDS main catalog with the 495 NSA dwarf galaxies in the eFEDS footprint, and arrive at a final sample of six dwarf galaxies with one associated eFEDS X-ray source per galaxy. See Sections 2.2 and 3.3 of Latimer et al. (2021a) for further details on the parent sample of dwarf galaxies and cross-matching parameters. All six of the galaxies exhibited moderately enhanced X-ray emission compared to their expected galaxy-wide contribution from XRBs based on the stellar mass and star formation rate of each galaxy, suggestive of accreting

massive BHs (see section 3.3 of Latimer et al. 2021a). They find X-ray source luminosities of $L_{0.5-8\text{keV}} \sim 10^{39-40} \text{ erg s}^{-1}$ across the galaxies in their sample.

Of the six dwarf galaxies in Latimer et al. (2021a) , we have selected three (IDs 1-3) to obtain new *Chandra X-ray Observatory* observations (Proposal ID: 23700654; PI: Kraft). *Chandra* supplies us with a finer spatial resolution ($\sim 1''$) than eROSITA ($\sim 16''$) (Predehl et al., 2021) for targets located at the aimpoint. It will allow us to constrain the locations and positional uncertainties of the X-ray sources previously detected in these galaxies, more accurately describe their X-ray emission, as well as fit spectra to determine further characteristics. We adopt ultraviolet+mid-IR star formation rates from Latimer et al. (2021a), based on the far-UV and mid-infrared luminosities via the relationships of Kennicutt & Evans (2012) and Hao et al. (2011). The properties of the three dwarf galaxies are summarized in Table 2.1, and images with the positions of their associated X-ray source are in Figure 2.1.

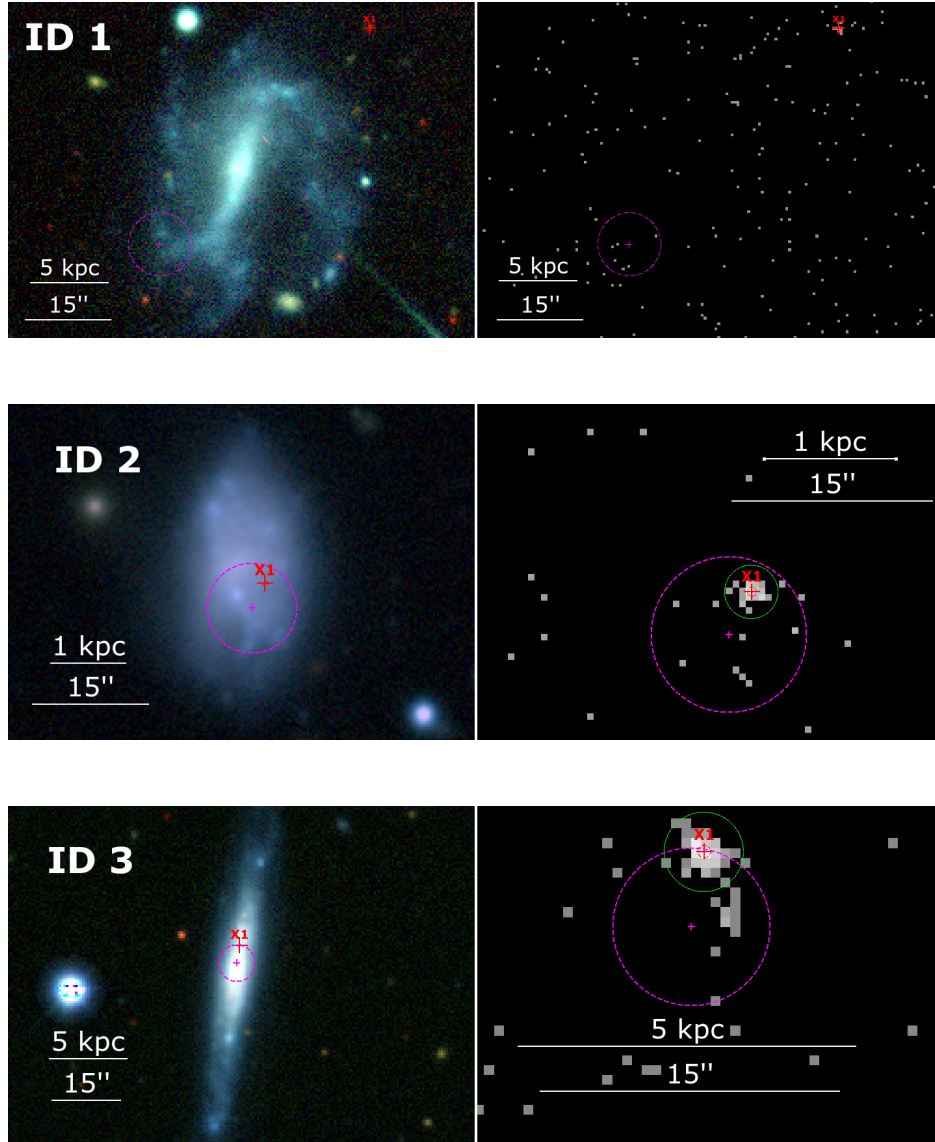


Figure 2.1: Left: Three-color images of our target galaxies retrieved from the Dark Energy Camera Legacy Survey (DECaLS; Dey et al. 2019) with the z , r , and g bands depicting red, green, and blue respectively. Right: *Chandra* X-ray images of the galaxies in the 2-10 keV band. We show the positions and the corrected combined positional uncertainty (based on the `RADEC_ERR_CORR` parameter from the eFEDS main catalog) in magenta. We also overlay the positions of our detected X-ray sources as red crosses. The green circles represent the $\sim 2''$ apertures around the sources. The red circle shows our new positional uncertainties regarding the X-ray sources. As can be seen, each one falls within the positional uncertainty reported in the eFEDS main catalog, except ID 1 which shows one of the off-galaxy X-ray sources detected.

Table 2.1. Sample Galaxy Properties

ID	NSAID	R.A.	Decl.	N_H	z	r_{50}	Distance	$\log M_*/M$	SFR
		(deg)	(deg)	(10^{20} cm^{-2})		(kpc)	(Mpc)		(M yr^{-1})
(1)	(2)	(3)	(4)	(5)	(6)	(7)	(8)	(9)	(10)
1	82162	140.942967	2.753302	3.58	0.0177	8.24	73	9.08	0.16
2	623354	145.180051	3.958864	3.64	0.0051	0.91	21	8.40	0.04
3	648474	141.572049	3.134800	3.82	0.0149	3.24	61	9.44	0.27

Note. — Table 2.1 information is taken from Latimer et al. (2021a). Column 1: Identification number used in Latimer et al. (2021a). Column 2: NSAIDs from v1.0.1 of the NSA. Column 3: R.A. of the galaxy. Column 4: Decl. of the galaxy. Column 5: Galactic neutral hydrogen density (Dickey & Lockman (1990); retrieved via <https://cxc.harvard.edu/toolkit/colden.jsp>). Column 6: Redshift, specifically the `zdist` parameter from the NSA. Column 7: Petrosian 50% light radius. Column 8: Galaxy distance. Column 9: log galaxy stellar mass ratio. Column 10: estimated SFRs from WISE data (see Section 3.3 Latimer et al. (2021a)). The values given in columns 6-9 are from the NSA and we assume $h = 0.73$.

Observations and Data Reduction

Target galaxy observations were taken with *Chandra* between 2022 March 06 and 2023 February 27, with exposure times ranging between 11.6 and 23.8 ks. Each observation was taken with the galaxy centered on the S3 chip of the Advanced CCD Imaging Spectrometer (ACIS). Refer to Table 2.2 for a summary of the *Chandra* observations. We carried out the data reduction utilizing the CIAO v.4.14 (Fruscione et al., 2006) software to reprocess and calibrate (CALDB v4.9.8) the data, creating new level 2 event files.

We aligned the astrometry of the *Chandra* observations to the SDSS catalog sources (DR12) for correction. First, we run the `wavdetect` CIAO function to identify and create a list of X-ray point sources, focused solely on the S3 chip filtered in the broad band between 0.5-7 keV. `wavdetect` is a point source detection algorithm that correlates the sources with “Mexican Hat” wavelet functions. Any sources found by the `wavdetect` algorithm that fall inside of $3r_{50}$ of the galaxy were excluded. The `wcs_match` function was then applied to match the sources that remained to *i*-band magnitude <22 optical point sources in the SDSS DR12. A minimum of one source match had to be found to correct the astrometry. Only translation corrections are applied given the small number of matches. The astrometry for only one of the three galaxies (ID 2) was corrected with a translation of ± 1.57 pixels ($0''.77$). We also remedy our images of any background flares. We take our astrometrically-corrected images and remove any time interval where the background rate is $>3\sigma$ using the `deflare` script.

Table 2.2. Chandra Observations

ID	Date Observed	Obs ID	Exp. Time (ks)	$N_{background}$
1	2022 Oct 13	26034	18.7	0.8680
	2022 Oct 16	27479	11.6	
2	2022 Mar 07	26035	12.9	0.1456
3	2023 Feb 27	26036	22.8	0.3561

Note. — $N_{background}$ is the expected number of hard band N ($>S$) background sources within our galaxy region ($3r_{50}$) using (Moretti et al., 2003).

Analysis and Results

X-ray Sources

From the Chandra X-ray data, we can search for signatures that may suggest the presence of accretion supported by a massive BH in any of our target galaxies. We run **wavdetect** again, isolating it to images from the S3 chip filtering them from 0.5-7 keV. We utilize the same parameters and methods in Section 4.1 of Latimer et al. (2021b), which will be detailed as follows. We adopt wavelet scales of 1.0, 1.4, 2.0, 2.8, and 4.0 coupled with a point spread function map at 39% with an enclosed energy fraction set at 2.3 keV (for the hard band; 2-7 keV) and 1.56 keV (for the soft band; 0.5-2 keV), setting our significance threshold to 10^{-6} (approximately one false source detection over the area of the S3 chip). We confine our analysis to only the **wavdetect** sources that fall within the $3r_{50}$ region to omit sources not associated with the target dwarf galaxies.

Within each galaxy region ($3r_{50}$) we detect 1-3 X-ray sources in each band. However, the sources detected for ID 1 lie far outside the optical extent of the galaxy, resulting in non-detections in both of the observations taken of the galaxy. The non-detection of the source previously detected in the eFEDS catalog persisted after merging the observations. For ID 2 and ID 3, we detect X-ray sources within the optical extent of the galaxies. We determine the positions of the X-ray sources are consistent with the X-ray source positions and positional uncertainties of Latimer et al. (2021a) (see Figure 2.1). The X-ray source found in ID 2 remains off-nuclear and the detection in ID 3 remains associated with the nucleus. We catalog the properties of the X-ray sources in Table 2.3.

The source counts are determined by applying circular apertures that enclose 90% of the enclosed energy fraction at 4.5 keV ($\sim 2''$). Additionally, we make use of circular annuli to estimate the background counts per pixel. The inner radius is set to the source aperture with an outer radius $12\times$ that of the inner. Following the methods detailed by Kraft et al.

(1991) for Poisson-distributed data for sources with low counts, we require the source counts to be above the background counts to within 95% confidence for the source to be detected. Afterwards, we subtract the background counts in the aperture from the source counts and apply a 90% aperture correction to attain the net counts for each source.

We use the CIAO function `srcflux` to get initial estimates of the X-ray fluxes from our targets in the hard (2-10 keV) and soft (0.5-2 keV) bands. We use a power-law spectrum model where we adopt a photon index of $\Gamma = 1.8$, which is common for low-luminosity AGN (Ho, 2008, 2009), and ultraluminous X-ray sources at these ranges (Swartz et al., 2008) with Galactic column densities from Dickey & Lockman (1990) maps. We report the unabsorbed fluxes and their luminosities in Table 2.3. As in Latimer et al. (2021b), we ignore potential absorption intrinsic to each source, therefore these values should be taken as lower limits. Our 2-10 keV X-ray band luminosities fall in the range $\log (L_{2-10\text{keV}}/\text{erg s}^{-1}) = 39.2\text{--}40.43$ (see Table 2.3). We find upper limits based on the minimum fluxes found for ID 1 to set upper limits on the X-ray source luminosities given the non-detection.

Table 2.3. X-Ray Sources

ID	R.A. (deg)	Dec. (deg)	Pos. Uncertainty (arcsec)	Net Counts			Flux (10^{-15} erg s $^{-1}$ cm $^{-2}$)		Luminosity (log[erg s $^{-1}$])	
				0.5-2 keV	0.5-7 keV	2-7 keV	0.5-2 keV	2-10 keV	0.5-2 keV	2-10 keV
(1)	(2)	(3)	(4)	(5)	(6)	(7)	(8)	(9)	(10)	(11)
1 ^a	<2.40	<5.23	<39.2	<39.5
2	145.179013	3.959214	0.35	28.49±9.7	45.12±12.15	15.25 ^{+8.67} _{-6.09}	27.43	29.72	39.16	39.20
3	141.571720	3.136256	0.32	57.25±13.45	113.69±18.74	58.07±13.82	32.58	59.89	40.16	40.43

Note. — Column 1: Identification number used in Latimer et al. (2021a). Column 2: R.A of the X-ray source. Column 3: Decl. of the X-ray source. Column 4: Positional Uncertainties for each source. Columns 5-7: Net counts after applying a 90% aperture correction. Error bars represent 90% confidence intervals. Column 8-9: Fluxes corrected for Galactic absorption. Column 10-11: Log luminosities corrected for Galactic absorption; calculated using a photon index of $\Gamma = 1.8$.

^a No soft and/or hard band X-ray sources were detected in these galaxies. The reported fluxes and luminosities are upper limits (see section 2).

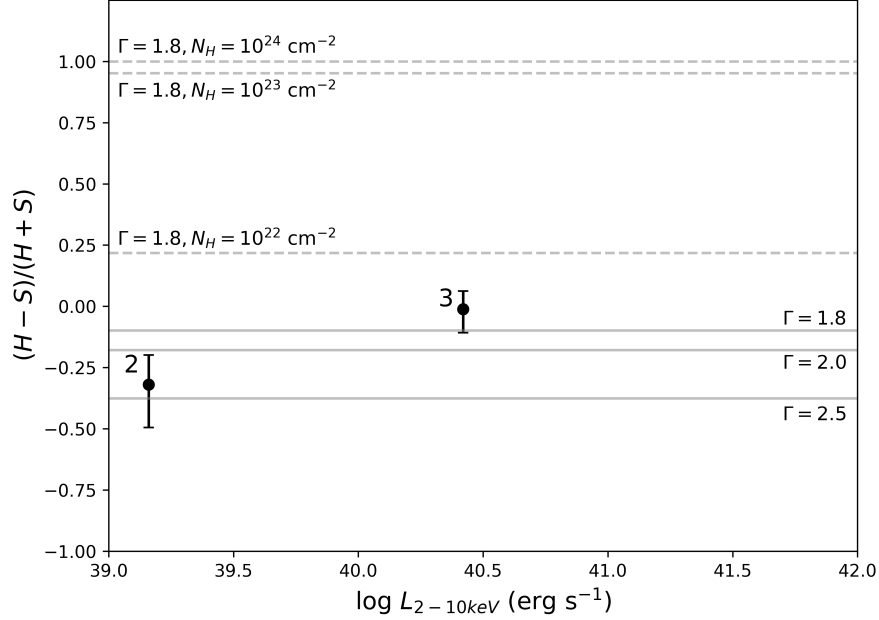


Figure 2.2: Hardness ratio vs. $\log 2\text{--}10$ keV X-ray luminosity for our two galaxies with a detected X-ray source in at least one of the two bands. The hardness ratio was calculated using BEHR (see Section 2). The error bars are the 68% confidence intervals. Hardness ratios for unabsorbed $\Gamma = 1.8, 2.0$, and 2.5 are depicted as solid gray lines, while the absorbed power laws with $\Gamma = 1.8$ are shown with gray dashed lines.

We next apply the code of Park et al. (2006) for the Bayesian Estimation of Hardness Ratios (BEHR). BEHR is a robust tool for estimating hardness ratios for sources within the Poisson regime of low counts. We follow the given definition of hardness ratio as $(H - S)/(H + S)$. H is the number of detected counts in the hard band and S is the number detected in the soft band. We define the hard X-ray band here as 2-7 keV and soft band as 0.5-2 keV. Of our three galaxies, only two are detected in both energy bands, the resulting hardness ratios shown in Figure 2.2. For comparison, we also estimate and plot the hardness ratios using the Portable, Interactive Mult-Mission Simulator (PIMMS)¹ for unabsorbed power laws with $\Gamma = 1.8, 2.0$, and 2.5 and for absorbed power laws with $\Gamma = 1.8$ and $N_H = 10^{22-24} \text{ cm}^{-2}$.

Furthermore, we estimate the number of background hard/soft X-ray sources that we

¹<https://heasarc.gsfc.nasa.gov/cgi-bin/Tools/w3pimms/w3pimms.pl>

expect may reside within $3r_{50}$ of our target galaxy. From Moretti et al. (2003), Equation (2) allows us to input a given flux, to which, it then outputs the the number of background sources we would expect that would have the given flux or higher that we should see (per square degree). We use our calculated minimum values for the flux that could be detected as a source, assuming two source counts that correspond to the weakest source detected in each energy band. Our ensuing minimum fluxes for our 3 observations lie in the range $S_{min} \sim 1.2$ -2 and $S_{min} \sim 2.3$ -4 for the 0.5-2 keV and 2-10 keV bands, respectively, with units of 10^{-15} erg s $^{-1}$ cm $^{-2}$. Now, from these fluxes we can calculate the expected number of background sources in the soft (hard) band inside $3r_{50}$ of our galaxies, of which, ranges from ~ 0.085 -0.525 (0.147-0.868).

X-ray Spectra

We model and fit the spectra of the X-ray sources detected with CIAO's built-in modelling and fitting package, **SHERPA** v.4.14 (Burke et al., 2021). We input the source and background regions (the circular annuli based on our source apertures) created earlier in the analysis (see Section 2) into the CIAO function **specextract**. The function creates the necessary auxiliary response and redistribution matrix files to plot our spectra for each source. Given the possibility of having both Galactic absorption and absorption intrinsic ($N_{H,int}$) to the target galaxies, we fit the spectra using two models: (i) an absorbed power-law model without intrinsic absorption (**xsphabs*xspowerlaw**) and (ii) an absorbed power-law with intrinsic absorption (**xphabs*xsphabs*xspowerlaw**). For both models, we make use of the Galactic column densities reported by Dickey & Lockman (1990), which we keep fixed. We allow all other parameters to vary and estimate the uncertainties to 68% confidence.

Based on the first model, we find that the spectrum of ID 2 has a best fit power law index of $\Gamma = 2.35^{+0.52}_{-0.45}$ and for the spectrum of ID 3 we find $\Gamma = 1.65^{+0.30}_{-0.29}$. When employing the second model, which takes into account an intrinsic component, ID 2 prefers an intrinsic

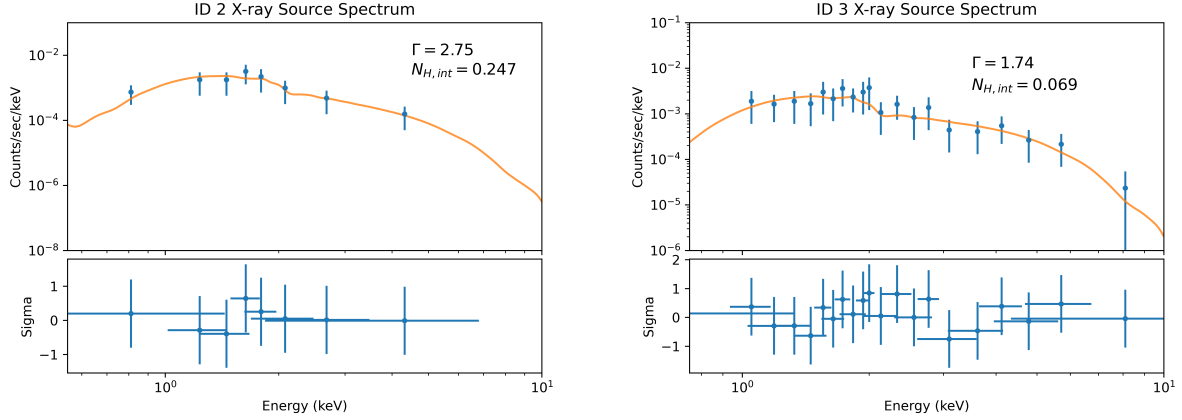


Figure 2.3: Summary of X-ray spectral fitting with reported Γ and intrinsic absorption values for the X-ray sources in ID 2 and ID 3. Left: X-ray source spectrum of ID 2. We fit the spectrum with an absorbed power-law model, finding a best fit $\Gamma = 2.75$ and $N_{H,int} = 0.247 \times 10^{22} \text{ cm}^{-2}$. Right: X-ray source spectrum of ID 3. We find the spectrum with an absorbed power-law model, finding the best fit $\Gamma = 1.74$ and $N_{H,int} = 0.069 \times 10^{22} \text{ cm}^{-2}$.

column of $N_{H,int} = 2.47 \times 10^{21} \text{ cm}^{-2}$, with a power-law index of $\Gamma = 2.75_{-0.81}^{+1.5}$. Likewise, the spectrum for ID 3 features a best-fit with an intrinsic absorption that is larger than its reported Galactic value with $N_{H,int} = 6.9 \times 10^{20} \text{ cm}^{-2}$, featuring a best fit power-law index of $\Gamma = 1.74_{-0.37}^{+0.71}$. Both ID 2 and ID 3 exhibit best-fit spectra that are suggestive of intrinsic absorption to some capacity. We show the spectrum for each galaxy, their best fit power law indexes, and intrinsic absorption values in Figure 2.3. We calculate unabsorbed 2-10 keV X-ray source fluxes and luminosities based on the modeled spectra and summarize the results in Table 2.4. The best fit power-law indexes for ID 2 and ID 3 from both models are also consistent with the hardness ratios calculated above with $\Gamma \approx 1.7$ and $\Gamma \approx 2.3$, respectively (see Figure 2.2). The X-ray source luminosities found whether via `srcflux` or fitting the spectra return values that are broadly consistent with values found in other studies concerning AGNs in dwarf galaxies (e.g. Baldassare et al., 2017; Mezcua et al., 2018; Reines et al., 2014).

Table 2.4. X-ray Source Properties From Fitting

ID	R.A.	Decl.	$F_{2-10kev}$	$\log L_{2-10kev}$
	(deg)	(deg)	(10^{-15} erg s $^{-1}$ cm $^{-2}$)	(erg s $^{-1}$)
(1)	(2)	(3)	(4)	(5)
2	145.179013	3.959214	23.34	39.09
3	141.572049	3.134800	54.98	40.39

Note. — Column 1: Identification number associated with the X-ray source. Column 2: R.A. of the X-ray source. Column 3: Decl. of the X-ray source. Column 4: Fluxes in the 2-10 keV band found from the modeled spectra corrected for any absorption. Column 5: log luminosity in 2-10 keV band, in erg s $^{-1}$.

Possible Origins of the X-ray Emission

X-ray Binaries. The luminosities we report for the detected X-ray sources in our target dwarf galaxies are not so high as to definitively rule out accretion onto stellar-mass BHs (or neutron stars) in XRBs. However, based on the eFEDS detections, Latimer et al. (2021a) found luminosities above the galaxy-wide expected contribution from XRBs. We revisit the analysis using our new high resolution *Chandra* data.

The expected X-ray luminosity from low-mass XRBs scales with stellar mass (Gilfanov, 2004) and their high-mass counterparts scale with SFR (Grimm et al., 2003; Mineo et al., 2012). We invoke the relation of Lehmer et al. (2010), which accounts for the expected galaxy-wide contribution of both low-mass and high-mass XRBs: $L_{2-10\text{keV}}^{XRB}(\text{erg s}^{-1}) = \alpha M_* + \beta \text{SFR}$ with $\alpha = (9.05 \pm 0.27) \times 10^{28} \text{ erg s}^{-1} M^{-1}$ and $\beta = (1.62 \pm 0.22) \times 10^{29} \text{ erg s}^{-1} (M \text{ yr}^{-1})^{-1}$. We plot the the unabsorbed X-ray luminosities of our sources from the spectral fitting versus the total expected X-ray luminosities in the host galaxies from XRBs in Figure 2.4. The measured luminosities are one to two orders of magnitude higher than that expected from XRBs, suggesting the presence of AGNs in our target galaxies. For the non-detection in ID 1, we plot the upper limit of our minimum luminosity found using `srcflux` from earlier.

Ultraluminous X-ray Sources. Next, we must take into consideration the likelihood of ultraluminous X-ray sources (ULXs) being the cause of the X-ray emissions detected in our sample. ULXs are described as being off-nuclear sources with X-ray luminosities above $10^{39} \text{ erg s}^{-1}$ (see Kaaret et al. (2017) for a review). Our source positions and their luminosities fall rather squarely into that definition. We refer to the analysis done by Latimer et al. (2021a) in which they incorporated line fluxes from the NSA (found for ID 2 and 3) and the SFRs they calculated to estimate the metallicity based on the relations from Greene & Ho (2004). Both galaxies were found to be of either intermediate or high metallicity. They

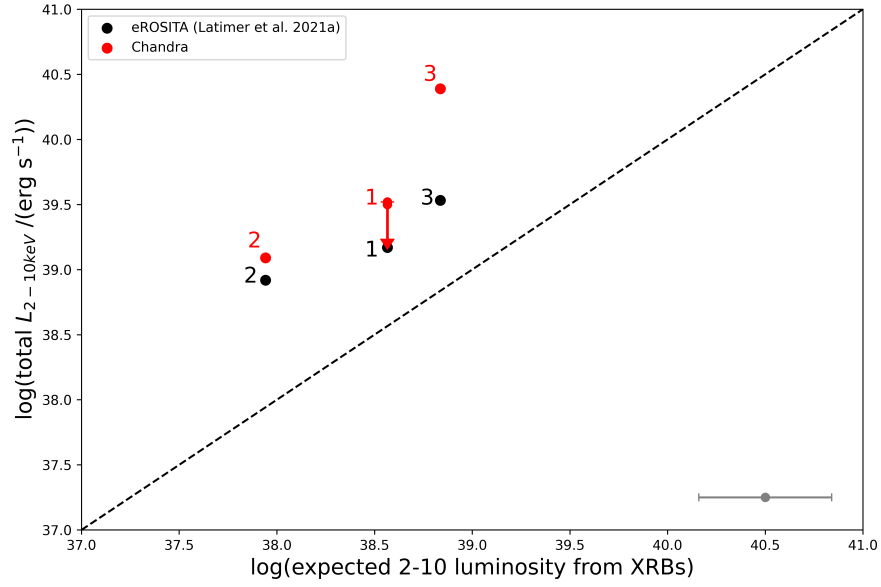


Figure 2.4: Total observed X-ray luminosities of the galaxies in our sample vs. what we would expect to see from XRBs via the relation of Lehmer et al. (2010). The black points are the values found by Latimer et al. (2021a) for comparison. The dashed line represents the one-to-one relation, and the scatter of 0.34 dex in the expected XRB luminosities is shown in grey to the bottom right. The error bars shown are 90% confidence intervals calculated via `srcflux`. Note: ID 1 is plotted using the upper limit of its minimum log luminosity.

also follow the findings of Swartz et al. (2004) and Mapelli et al. (2010) to determine the expected number of ULXs based on relations to SFR and galaxy mass, resulting in ~ 1 ULX across their sample of six galaxies. There is a low likelihood that both of the sources we have detected are ULXs.

Massive Black Holes. If we assume the X-ray luminosities we have measured are due to accreting massive BHs, we can perform calculations to estimate their Eddington ratios. The Eddington ratio of an accreting BH is found via

$$f_{Edd} = (\kappa L_X)/(L_{Edd}) \quad (2.1)$$

where κ is the hard (2-10 keV) bolometric correction, L_X is the hard X-ray luminosity of the BH, and L_{Edd} is the Eddington luminosity of the BH, which is given by

$$L_{Edd} \approx 1.26 \times 10^{38} \frac{M_{BH}}{M_\odot} \text{ erg s}^{-1}. \quad (2.2)$$

The BH masses are estimated using Equation (4) from Reines & Volonteri (2015), which gives the $\log(M_{BH})$ as a function of total host galaxy stellar mass, $\log(M_{stellar})$, for local AGNs. The resultant BH masses are $\log(M_{BH}/M_\odot) \approx 5.3$, 4.7, and 5.8 for ID 1, 2, and 3 respectively.

We invoke Equation (3) of Duras et al. (2020) for the hard X-ray bolometric corrections returning a mean $L_{Bol}/L_{2-10keV} \cong 15.33$. Note that for ID 1 we are using the upper limit given the non-detection. Combining these values in the usual way, we find Eddington fractions of $\sim 0.1\%$, $\sim 0.3\%$, and $\sim 0.5\%$.

Comparison with Latimer et al. (2021a)

To properly compare the X-ray luminosities from eROSITA presented by Latimer et al. (2021a) with our values from *Chandra*, we must adopt the same parameters in the analysis. To be consistent with Latimer et al. (2021a), we estimate source fluxes using a photon index of $\Gamma = 2.0$ and Galactic absorption of $3.0 \times 10^{20} \text{ cm}^{-2}$. We also run through our analysis in the 0.5-8 keV band.

Immediately something of note arises, that being an increase of ~ 0.34 and ~ 0.73 dex

from the Latimer et al. values of the 0.5-8 keV log luminosities for ID 2 and ID 3, respectively. In other words, the luminosity of ID 2 more than doubled and the source in ID 3 increased its luminosity by a factor of more than 5 between our study and theirs. This increase can be seen in Figure 2.4 comparing the *Chandra* and eROSITA observations, but in the 2-10 keV range.

It is a common feature of AGNs to exhibit variability at X-ray wavelengths. The timescales for such variability can extend anywhere from minutes to years. Even in low mass hosts, we see evidence of this wide variability (e.g. Baldassare et al. 2017; Ludlam et al. 2015; Yang et al. 2016).

Summary and Conclusions

We analyze *Chandra* observations of 3 AGN candidates in dwarf galaxies identified in Latimer et al. (2021a) using eFEDS data from eROSITA. Two galaxies had detections of X-ray sources within the positional uncertainty reported by eFEDS. The other target galaxy had no X-ray source detected at the eFEDS position. Our main findings are summarized below:

- The detected X-ray sources for our galaxies are bright with $L_{2-10} \sim 1 \times 10^{39}$ erg s $^{-1}$ for ID 2 and 2×10^{40} erg s $^{-1}$ for ID 3.
- The X-ray spectra are well-described by absorbed power-law models with $\Gamma = 2.75$; $N_H = 2.47 \times 10^{21}$ cm $^{-2}$ for ID 2 and $\Gamma = 1.74$; $N_H = 6.9 \times 10^{20}$ cm $^{-2}$ for ID 3, where N_H refers to absorption intrinsic to the source.
- The detected X-ray sources are unlikely to be low-mass or high-mass X-ray binaries given the luminosities are at least an order of magnitude higher than the expected galaxy-wide emission from XRBs. There is also a low chance they are both resulting from ULXs.
- If the detected X-ray sources are due to active massive BHs with masses that scale with the stellar mass of their host galaxies ($M_{\text{BH}} \sim 10^5$ to 10^6), we infer Eddington ratios of ~ 0.003 and ~ 0.005 for ID 2 and ID 3 respectively.
- The X-ray source fluxes and luminosities are $\sim 2 - 5\times$ higher than their initial detections in Latimer et al. (2021a). Such long-term X-ray variability is a common feature of AGNs.

The three dwarf galaxies studied here originally come from a sample of six total identified by Latimer et al. (2021a). Follow-up high resolution X-ray observations, like

in this work, of the remaining three galaxies would allow us to verify the AGN fraction in dwarf galaxies based on the eFEDS catalog. Moreover, follow-up observations at other wavelengths could provide meaningful information to assist in distinguishing between XRBs and massive BHs in our target galaxies. High resolution radio observations could locate radio sources that may coincide with our detected X-ray sources. Combining X-ray and radio observations have already been used to reveal massive BHs in dwarf galaxies (e.g. Reines et al., 2011) since massive BHs are much more luminous than XRBs in the radio. Analysis of spatially-resolved optical line spectra would provide additional diagnostics by analyzing broad and narrow emission lines looking for AGN signatures. A multiwavelength approach to the study of AGNs in dwarf galaxies ultimately leads to a better understanding of these phenomena.

CONCLUSION

In summary, we have used the advantages that come with observations in the X-ray wavelength to probe, analyze, and search three dwarf galaxies for active massive black holes. Supermassive black holes (SMBHs) are ubiquitous in the Universe as they inhabit the centers of roughly all massive galaxies. They are a fundamental aspect to both the structure of a galaxy but also in the way it evolves, yet their origins remain obscured. Understanding how SMBHs form grant us a better comprehension of the relationship between the SMBH and the host galaxy, gravitational waves, TDEs, and accretion. Theorists have proposed formation scenarios to explain their origins, but they are difficult to verify given our current technology's inability to look back to such high redshifts. We must find other avenues to investigate.

Through the observation and study of dwarf galaxies, nearby and plenty in number, we may be able to constrain the formation mechanism(s) that took place to create massive black hole seeds, which would eventually grow into their modern day supermassive sizes. Dwarf galaxies present an analog to early-universe galaxies based on their relatively quiet merger histories. They provide us with the chance to study a range of galaxy properties, how they relate to BHs, and may even house remnant massive BHs left over from the early universe.

Accreting BHs in the centers of galaxies give rise to AGNs, which emit light across the entire electromagnetic spectrum. Hunting for AGN in dwarf galaxies reveal to us the likely presence of a BH at its core. Accretion characteristically generates X-rays that can be investigated to reveal the properties of the BH powering an AGN.

In Chapter 2, we used new high resolution *Chandra X-ray Observatory* data to take a deeper, more pinpoint view at a sample of AGN candidate dwarf galaxies, in the hopes of corroborating signatures detected by Latimer et al. (2021a) for the presence of BHs. We are largely able to add confidence to the likelihood these X-ray sources, originally from the

eFEDS catalog, may indeed be weakly accreting massive BH.

In utilizing the robust and multi-faceted CIAO data analysis package we were able to calculate net counts, fluxes, and luminosities for the three galaxies and found they were suggestive of AGN activity. We managed to have enough counts for two sources to fit spectra. From the fitting, we found that each source was experiencing absorption intrinsic to their galaxies in varying degrees. We also calculated hardness ratios which supported the values found through fitting. We did not detect an X-ray source within the optical extent of one of the three galaxies, but were still able to find the minimum fluxes and, therefore luminosities to constitute a detection.

The process has illuminated the key challenges when searching for massive black holes in dwarf galaxies, that being that the signatures characteristic of AGN in dwarf galaxies are not unique to this sole group, particularly in the X-ray. Concerning their SMBH relatives who can generate fluxes so powerful it immediately rules out the possibility of any other astrophysical phenomena, XRBs and ULXs can produce signatures that appear to mimic active massive BHs.

Given the relative sizes for massive BHs in comparison to SMBHs, they produce luminosities that are demonstrably weaker. Differentiating between an XRB undergoing super-Eddington accretion and a weakly accreting massive BH, for example, often times requires observations in more than one wavelength to properly investigate. Scaling relations also provide additional information in being able to at least determine the likelihood of an X-ray source in a galaxy being a result of XRBs or ULXs. Based on those very scaling relations we do determine our sources may more than likely be due to AGN presence in these dwarf galaxies.

More can be done to better determine and hopefully confirm the presence of a massive BH in our sample of dwarf galaxies. We can study the optical spectra of these galaxies in search of broad $H\alpha$ emission to form better BH mass estimates, and narrow line emissions

from photo-ionized gas characteristic of AGNs. Observations in the radio can be used to find sources coincident with detected X-ray sources as AGN are brighter in the radio than XRBs. Ultraviolet observations can tell us more about the radiative properties and together with X-rays can tell us more about the accretion disk itself and the corona.

The hunt for AGN in dwarf galaxies is a multiwavelength endeavor and as the field progresses more possibilities will arise to apply this approach. The eROSITA All-Sky Survey, mentioned earlier (Chapter 1), will very soon facilitate analysis in the X-ray of an ample sample size of potential AGN. The newly deployed *James Webb Space Telescope (JWST)* will be able to observe farther into the early universe and with higher resolution, opening the doors to more IR studies remedying some of the issues with mid-IR color-color selection. In the slightly farther future the *Laser Interferometer Space Antenna (LISA)* could reveal, at least partially, answers to our long held questions on the origins of supermassive black holes by using gravitational waves to detect BH mergers out to very high redshift. Together, all of this new data could provide better constraints on the formation mechanism(s), occupation fraction, and scaling relations for AGN in dwarf galaxies. Every study contributes to this fascinating and growing body of work dedicated to studying AGNs and the dwarf galaxies they reside in. It paves the way for new technologies and new ideas that will support the many discoveries to come.

REFERENCES CITED

- Bañados, E., Venemans, B. P., Mazzucchelli, C., et al. 2018, , 553, 473, doi: 10.1038/nature25180
- Baldassare, V. F., Reines, A. E., Gallo, E., & Greene, J. E. 2017, , 836, 20, doi: 10.3847/1538-4357/836/1/20
- Birchall, K. L., Watson, M. G., & Aird, J. 2020, , 492, 2268, doi: 10.1093/mnras/staa040
- Brandt, W. N., & Alexander, D. M. 2015, , 23, 1, doi: 10.1007/s00159-014-0081-z
- Bromm, V., & Larson, R. B. 2004, , 42, 79, doi: 10.1146/annurev.astro.42.053102.134034
- Brunner, H., Liu, T., Lamer, G., et al. 2022, , 661, A1, doi: 10.1051/0004-6361/202141266
- Burke, D., Laurino, O., Wmclaugh, et al. 2021, sherpa/sherpa: Sherpa 4.14.0, 4.14.0, Zenodo, Zenodo, doi: 10.5281/zenodo.5554957
- Dey, A., Schlegel, D. J., Lang, D., et al. 2019, , 157, 168, doi: 10.3847/1538-3881/ab089d
- Dickey, J. M., & Lockman, F. J. 1990, , 28, 215, doi: 10.1146/annurev.aa.28.090190.001243
- Duras, F., Bongiorno, A., Ricci, F., et al. 2020, , 636, A73, doi: 10.1051/0004-6361/201936817
- Fan, X., Carilli, C. L., & Keating, B. 2006, , 44, 415, doi: 10.1146/annurev.astro.44.051905.092514
- Fruscione, A., McDowell, J. C., Allen, G. E., et al. 2006, in Society of Photo-Optical Instrumentation Engineers (SPIE) Conference Series, Vol. 6270, Observatory Operations: Strategies, Processes, and Systems, ed. D. R. Silva & R. E. Doxsey, 62701V, doi: 10.1117/12.671760
- Fryer, C. L., Woosley, S. E., & Heger, A. 2001, , 550, 372, doi: 10.1086/319719
- Gallo, E., Treu, T., Jacob, J., et al. 2008, , 680, 154, doi: 10.1086/588012
- Gilfanov, M. 2004, , 349, 146, doi: 10.1111/j.1365-2966.2004.07473.x
- Greene, J. E., & Ho, L. C. 2004, , 610, 722, doi: 10.1086/421719
- Greene, J. E., Strader, J., & Ho, L. C. 2020, , 58, 257, doi: 10.1146/annurev-astro-032620-021835

- Grimm, H. J., Gilfanov, M., & Sunyaev, R. 2003, , 339, 793, doi: 10.1046/j.1365-8711.2003.06224.x
- Hao, C.-N., Kennicutt, R. C., Johnson, B. D., et al. 2011, , 741, 124, doi: 10.1088/0004-637X/741/2/124
- Hickox, R. C., Jones, C., Forman, W. R., et al. 2009, , 696, 891, doi: 10.1088/0004-637X/696/1/891
- Ho, L. C. 2008, , 46, 475, doi: 10.1146/annurev.astro.45.051806.110546
- . 2009, , 699, 626, doi: 10.1088/0004-637X/699/1/626
- Inayoshi, K., Visbal, E., & Haiman, Z. 2020, , 58, 27, doi: 10.1146/annurev-astro-120419-014455
- Jiang, Y.-F., Stone, J. M., & Davis, S. W. 2019, , 880, 67, doi: 10.3847/1538-4357/ab29ff
- Kaaret, P., Feng, H., & Roberts, T. P. 2017, , 55, 303, doi: 10.1146/annurev-astro-091916-055259
- Karlsson, T., Bromm, V., & Bland-Hawthorn, J. 2013, Reviews of Modern Physics, 85, 809, doi: 10.1103/RevModPhys.85.809
- Kauffmann, G., Heckman, T. M., Tremonti, C., et al. 2003, , 346, 1055, doi: 10.1111/j.1365-2966.2003.07154.x
- Kelly, B. C., & Merloni, A. 2012, Advances in Astronomy, 2012, 970858, doi: 10.1155/2012/970858
- Kennicutt, R. C., & Evans, N. J. 2012, , 50, 531, doi: 10.1146/annurev-astro-081811-125610
- Kimbro, E., Reines, A. E., Molina, M., Deller, A. T., & Stern, D. 2021, , 912, 89, doi: 10.3847/1538-4357/abec6a
- Kolodzig, A., Gilfanov, M., Sunyaev, R., Sazonov, S., & Brusa, M. 2013, , 558, A89, doi: 10.1051/0004-6361/201220880
- Kraft, R. P., Burrows, D. N., & Nousek, J. A. 1991, , 374, 344, doi: 10.1086/170124
- Latif, M. A., & Ferrara, A. 2016, , 33, e051, doi: 10.1017/pasa.2016.41
- Latif, M. A., Schleicher, D. R. G., Schmidt, W., & Niemeyer, J. 2013, , 430, 588, doi: 10.1093/mnras/sts659
- Latimer, L. J., Reines, A. E., Bogdan, A., & Kraft, R. 2021a, , 922, L40, doi: 10.3847/2041-8213/ac3af6

- Latimer, L. J., Reines, A. E., Hainline, K. N., Greene, J. E., & Stern, D. 2021b, , 914, 133, doi: 10.3847/1538-4357/abfe0c
- Lehmer, B. D., Alexander, D. M., Bauer, F. E., et al. 2010, , 724, 559, doi: 10.1088/0004-637X/724/1/559
- Lemons, S. M., Reines, A. E., Plotkin, R. M., Gallo, E., & Greene, J. E. 2015, , 805, 12, doi: 10.1088/0004-637X/805/1/12
- Lodato, G., & Natarajan, P. 2006, , 371, 1813, doi: 10.1111/j.1365-2966.2006.10801.x
- Ludlam, R. M., Cackett, E. M., Gültekin, K., et al. 2015, , 447, 2112, doi: 10.1093/mnras/stu2618
- Mapelli, M., Ripamonti, E., Zampieri, L., Colpi, M., & Bressan, A. 2010, , 408, 234, doi: 10.1111/j.1365-2966.2010.17048.x
- Mezcua, M., Civano, F., Marchesi, S., et al. 2018, , 478, 2576, doi: 10.1093/mnras/sty1163
- Mineo, S., Gilfanov, M., & Sunyaev, R. 2012, , 419, 2095, doi: 10.1111/j.1365-2966.2011.19862.x
- Moretti, A., Campana, S., Lazzati, D., & Tagliaferri, G. 2003, , 588, 696, doi: 10.1086/374335
- Mortlock, D. J., Warren, S. J., Venemans, B. P., et al. 2011, , 474, 616, doi: 10.1038/nature10159
- Mushotzky, R. 2004, in *Astrophysics and Space Science Library*, Vol. 308, *Supermassive Black Holes in the Distant Universe*, ed. A. J. Barger, 53, doi: 10.1007/978-1-4020-2471-9_2
- Nucita, A. A., Manni, L., De Paolis, F., Giordano, M., & Ingrosso, G. 2017, , 837, 66, doi: 10.3847/1538-4357/aa5f4f
- Omukai, K. 2001, , 546, 635, doi: 10.1086/318296
- Pardo, K., Goulding, A. D., Greene, J. E., et al. 2016, , 831, 203, doi: 10.3847/0004-637X/831/2/203
- Park, T., Kashyap, V. L., Siemiginowska, A., et al. 2006, , 652, 610, doi: 10.1086/507406
- Predehl, P., Andritschke, R., Arefiev, V., et al. 2021, , 647, A1, doi: 10.1051/0004-6361/202039313
- Reines, A. E. 2022, *Nature Astronomy*, 6, 26, doi: 10.1038/s41550-021-01556-0
- Reines, A. E., Greene, J. E., & Geha, M. 2013, , 775, 116, doi: 10.1088/0004-637X/775/2/116

- Reines, A. E., Plotkin, R. M., Russell, T. D., et al. 2014, , 787, L30, doi: 10.1088/2041-8205/787/2/L30
- Reines, A. E., Reynolds, M. T., Miller, J. M., et al. 2016, , 830, L35, doi: 10.3847/2041-8205/830/2/L35
- Reines, A. E., Sivakoff, G. R., Johnson, K. E., & Brogan, C. L. 2011, , 470, 66, doi: 10.1038/nature09724
- Reines, A. E., & Volonteri, M. 2015, , 813, 82, doi: 10.1088/0004-637X/813/2/82
- She, R., Ho, L. C., & Feng, H. 2017, , 835, 223, doi: 10.3847/1538-4357/835/2/223
- Silk, J. 2017, , 839, L13, doi: 10.3847/2041-8213/aa67da
- Swartz, D. A., Ghosh, K. K., Tennant, A. F., & Wu, K. 2004, , 154, 519, doi: 10.1086/422842
- Swartz, D. A., Soria, R., & Tennant, A. F. 2008, , 684, 282, doi: 10.1086/587776
- Thygesen, E., Plotkin, R. M., Soria, R., et al. 2023, , 519, 5848, doi: 10.1093/mnras/stad002
- Truemper, J. 1993, *Science*, 260, 1769, doi: 10.1126/science.260.5115.1769
- Visbal, E., Haiman, Z., & Bryan, G. L. 2014, , 442, L100, doi: 10.1093/mnrasl/slu063
- Volonteri, M. 2010, , 18, 279, doi: 10.1007/s00159-010-0029-x
- Wise, J. H., Regan, J. A., O'Shea, B. W., et al. 2019, , 566, 85, doi: 10.1038/s41586-019-0873-4
- Yang, G., Brandt, W. N., Luo, B., et al. 2016, , 831, 145, doi: 10.3847/0004-637X/831/2/145